Impact of Swell on Air–Sea Momentum Flux and Marine Boundary Layer under Low-Wind Conditions

QINGFANG JIANG

Naval Research Laboratory, Monterey, California

PETER SULLIVAN

National Center for Atmospheric Research, Boulder, Colorado

SHOUPING WANG AND JAMES DOYLE

Naval Research Laboratory, Monterey, California

LINWOOD VINCENT

UCAR Visiting Scientist Programs, Monterey, California

(Manuscript received 15 July 2015, in final form 23 March 2016)

ABSTRACT

The impact of fast-propagating swell on the air–sea momentum exchange and the marine boundary layer is examined based on multiple large-eddy simulations over a range of wind speed and swell parameters in the light-wind–fast-wave regime. A wave-driven supergeostrophic jet forms near the top of the wave boundary layer when the forwarding-pointing (i.e., negative) form drag associated with fast wind-following swell overpowers the positive surface shear stress. The magnitude of the form drag increases with the wavelength and slope and decreases with increasing wind speed, and the jet intensity in general increases with the magnitude of the surface form drag. The resulting negative vertical wind shear above the jet in turn enhances the turbulence aloft. The level of the wind maximum is found to be largely determined by the wavenumber and the ratio of the surface shear stress and form drag: the larger the magnitude of this ratio, the higher the altitude of the wind maximum.

Although the simulated wind profile often closely follows the log law in the wave boundary layer, the surface stress derived from the logarithmic wind profile is significantly larger than the actual total surface stress in the presence of swell. Therefore, the Monin–Obukhov similarity theory is generally invalid over swell-dominated ocean. This is attributed to the wave-induced contribution to momentum flux, which decays roughly exponentially in the vertical and is largely independent of local wind shear.

1. Introduction

Although our understanding of air–sea interaction processes has been advanced significantly over the past few decades, some fundamental issues remain to be resolved. One such issue is the interaction between the wave boundary layer (WBL, a relatively shallow layer adjacent to the water surface, where the wave-induced stress accounts for an appreciable portion of the total stress) and underlying fast-propagating swell. Previous studies based on laboratory experiments, field observations, and numerical simulations suggest that the interaction between swell and the atmospheric WBL may lead to dramatic changes in the surface stress and consequently modulate wind and turbulence profiles in the boundary layer. Under certain conditions, the total surface stress (i.e., the sum of the wave form drag and shear stress, and the latter is always positive) may approach zero or even become negative. A negative surface stress implies an upward transfer of momentum (i.e., from sea to air), which may lead to the formation of a supergeostrophic jet near the top of the WBL

Corresponding author address: Qingfang Jiang, Naval Research Laboratory, 7 Grace Hopper Ave., Monterey, CA 93940-5502.
E-mail: jiang@nrlmry.navy.mil

DOI: 10.1175/JAS-D-15-0200.1

(often referred to as wave-driven wind jet). The negative stress (i.e., momentum flux from sea to air) right above the sea surface has been documented by several field observation programs (Smedman et al. 1994; Drennan et al. 1999; Grachev and Fairall 2001). The upward momentum transfer from narrow-band waves mechanically generated in a laboratory has been reported by Harris (1966) and Lai and Shemdin (1971). The presence of a wind speed maximum in the WBL over swell has been noted by a few groups as well. For example, Smedman et al. (1999) found that, under light-wind and fast-swell conditions, the momentum flux near the surface is negligible and the mechanical production of turbulence is close to zero. Light-wind and fast-swell conditions (i.e., $U_{10}/c < 1$, where U_{10} is the 10-m wind speed and c is the swell phase speed) frequently occur over tropical areas, associated with swell generated by tropical cyclones or extratropical storms thousands of kilometers away (Hanley et al. 2010; Semedo et al. 2011). The swell may have significant impact on the air–sea exchange of heat and momentum, which in turn modify the turbulence and wind profiles in the boundary layer. Therefore, understanding the interaction between swell and the atmospheric boundary layer flow over tropical areas is of great importance to climate modeling (e.g., Carlsson et al. 2009).

Besides field observations and laboratory experiments, our understanding of turbulent flows over traveling swell has benefited greatly from numerical simulations using either sophisticated turbulence and wave resolving numerical models or lower-order analytical models. In the past 15 yr, several direct numerical simulation (DNS) studies have been conducted to investigate turbulent shearing flows over a moving wavy surface (e.g., Sullivan et al. 2000; Sullivan and McWilliams 2002; Rutgersson and Sullivan 2005; Kihara et al. 2007). The flow Reynolds number for these studies (i.e., generally around 10^4 or less) is still well below values in the real atmosphere. It is still computationally too expensive to simulate these phenomena using a DNS model with a realistic Reynolds number. Nevertheless, results from these studies were often found to be in qualitative agreement with existing observations and some analytical solutions (e.g., in terms of momentum fluxes and wind profiles). More recently, the response of a boundary layer to traveling surface waves has been examined by Sullivan et al. (2008), Nilsson et al. (2012), Yang et al. (2013), and Sullivan et al. (2014) using a large-eddy simulation (LES) model. Their simulations were able to reproduce many salient features observed in the atmospheric boundary layer, including the formation of a wave-driven wind jet, downward momentum flux above the jet, and the surface stress negated by the form drag.

In addition, using a one-dimensional boundary layer model with a parameterized wave-related stress profile, Hanley and Belcher (2008) and Semedo et al. (2009) demonstrated that when the negative form drag overpowers the shear stress near the surface, a wave-driven jet forms in the WBL with momentum transported downward above the wind maximum and upward below. The former focused on how form drag modified an Ekman boundary layer and the latter further simplified the problem by ignoring Earth's rotation. The model solutions in Hanley and Belcher (2008) also suggested that while the WBL depth was considered only a few multiples of the characteristic wave height, the swell impact can propagate throughout the whole boundary layer.

While all these aforementioned studies brought new insight into this complex problem, many questions remain to be answered, ranging from fundamental swell–WBL interaction dynamics to surface flux parameterizations for different sea states. The objective of this study is to shed light on the nature of the dynamical interaction between the WBL with relatively light winds over fast-moving swell. Specifically, we explore further the formation mechanism and characteristics of wave-driven wind jets above wind-following swell. While the light-wind and fast-wave regime has been examined by several LES studies (e.g., Sullivan et al. 2008, 2014), this paper distinguishes itself from the existing literature by focusing on the swell–WBL interaction and its dependence on swell and wind parameters. This is achieved through exploring a relatively large parameter space and analyzing multiple simulations with the wave parameters being varied systematically. The remainder of this paper is organized as the follows. The large-eddy simulation model and model configuration are described in section 2. The results from LESs are presented in section 3. Sections 4 and 5 contain the discussion and concluding remarks, respectively.

2. LES model and configuration

The LES model solves the incompressible Boussinesq equations (e.g., Moeng 1984; Sullivan et al. 2014) utilizing pseudospectral spatial discretization in surface-following coordinates with subgrid-scale (SGS) parameterizations outlined by Deardorff (1972) and Moeng and Wyngaard (1988). The swell is simplified as a monochromatic wave at the surface, which propagates at the phase speed of a linear deep-water wave. The physical domain (i.e., x, y, z) with a wavy time-dependent lower boundary is first transformed into the computational domain using surface-fitted curvilinear coordinates, (ξ, η, ζ). The model

TABLE 1. List of simulations and derived parameters for group A with the CTRL highlighted in bold. The parameters are wavelength (λ), wave age (c/U_g), surface friction velocity (u_s*), friction velocity derived from the profile method (u_p*), pressure stress e-folding decay coefficient (α_p), 10-m wind speed (U_{10}), maximum wind speed (U_m), nondimensional wind speed maximum level (kz_m), and drag coefficients derived from surface shear stress ($C_{d,10,s}$), total surface stress ($C_{d,10,t}$), and profile method ($C_{d,10,p}$).

Expt	λ (m)	c/U_g	u_s* (m s^{-1})	u_p* (m s^{-1})	α_p	U_{10} (m s^{-1})	U_m (m s^{-1})	kz_m	$C_{d,10,s}$ ($\times 10^{-3}$)	$C_{d,10,t}$ ($\times 10^{-3}$)	$C_{d,10,p}$ ($\times 10^{-3}$)
L032	32	2.35	0.124	0.105	1.75	2.90	2.93	3.50	1.8	−0.15	1.3
L064	64	3.33	0.150	0.154	1.28	3.51	3.57	1.75	1.8	−0.54	1.9
L128	**128**	**4.71**	**0.160**	**0.208**	**1.05**	**3.85**	**4.00**	**0.94**	**1.7**	**−1.2**	**2.9**
L256	256	6.67	0.170	0.254	1.04	3.73	4.35	0.70	2.1	−2.3	4.6
FLAT	—	0	0.084	0.089	—	2.26	3.00	—	1.4	1.4	1.5

equations are formulated in strong conservation form and discretized using pseudospectral methods in horizontal planes and second-order finite differences in the vertical. The equations are advanced in time using a third-order Runge–Kutta method. Further description of the numerical details of this model can be found in Sullivan et al. (2008, 2014).

The model domain contains 256 by 128 grid points in the x and y directions with a grid spacing of $\Delta x = \Delta y = 4$ m (therefore, the domain has a length, $L_x = 1024$ m, and a width, $L_y = 512$ m, with periodic boundary conditions applied along lateral boundaries). The domain depth is $L_z = 800$ m with 128 grid points in the vertical and the minimal grid spacing $\Delta\zeta_1 = 1$ m at the first model level. The vertical grid spacing increases gradually with altitude following $\Delta\zeta_{i+1}/\Delta\zeta_i \simeq \gamma$, where the stretching constant $\gamma \approx 1.01$. The model is initialized with a unidirectional vertically uniform wind, $\mathbf{V}(z) = (U_g, 0)$, in geostrophic balance with the Coriolis parameter $f = 10^{-4}$ s^{-1}. Here U_g denotes the geostrophic wind speed along the x direction. The airflow above the boundary layer remains in geostrophic balance throughout these simulations. The atmosphere is initially neutrally stratified (i.e., $d\theta/dz$, where θ is the potential temperature) below a reference level, $Z_i = 300$ m, above which the potential temperature linearly increases with height by 1 K every 100 m. The initially neutral layer allows for the rapid development of turbulence in the boundary layer and therefore reduces the model spinup time. Test simulations indicate that the wave boundary layer and surface fluxes are relatively insensitive to the choice of Z_i and the stability in the atmosphere above Z_i.

The monochromatic swell is described by $z_b(x, t) = a\sin k(x - ct)$ where z_b is the vertical displacement of the wave surface, a is the wave height, $k = 2\pi/\lambda$ is the swell wavenumber, and λ is the wavelength. The swell propagates along the x direction with a deep-water wave phase speed $c = \sqrt{g/k}$, where g is the gravity acceleration. In this study, a positive (negative) U_g corresponds to wind-following (opposing) swell. A small surface roughness length, $z_0 = 2 \times 10^{-4}$ m, is used as a crude representation of the molecular viscosity and unsolved wave effects. The surface heat flux is zero in all the simulations and consequently the surface layer (where the shear stress is nearly constant and tens of meters deep) is neutrally stratified. To achieve a statistically equilibrium solution, each simulation is carried out for 5 h, which is significantly longer than typical turbulence time scales. Most of the profiles and statistics presented in this study are averaged over a 15-min interval around $T = 5$ h. The model time step is limited by the Courant–Friedrichs–Levy (CFL) condition, and the maximum CFL number calculated using the ratio of the horizontal (vertical) grid spacing and the maximum horizontal (vertical) wind speed is set to be 0.5. The resulting time step varies from around ~0.6 s for short and gentle swell simulations to ~0.06 s for steep swell simulations.

A total of 15 LESs have been carried out to explore the impact of swell on the atmospheric boundary layer over a range of wavelength and slopes as well as geostrophic wind speeds. These simulations use the same model configuration except for different swell wavelength (group A), wave slope (group B), or geostrophic winds (group C).

3. Results

The model results are summarized in sections 3a, 3b, and 3c. Our focus is on (i) the influence of swell on air–sea momentum exchange and atmospheric wind and turbulence profiles, (ii) the impact of swell on the surface layer, and (iii) the variation of swell impact with varying wave parameters, which have not been systematically explored in prior studies.

a. Wavelength effect

Shown in Table 1 are a list of parameters (definitions are given in the following text) derived from the group A simulations corresponding to a geostrophic wind speed $U_g = 3$ m s^{-1}, swell slope $s = ak = 0.1$, and wavelength $\lambda = 32, 64, 128$, and 256 m (denoted as L032, L064, L128,

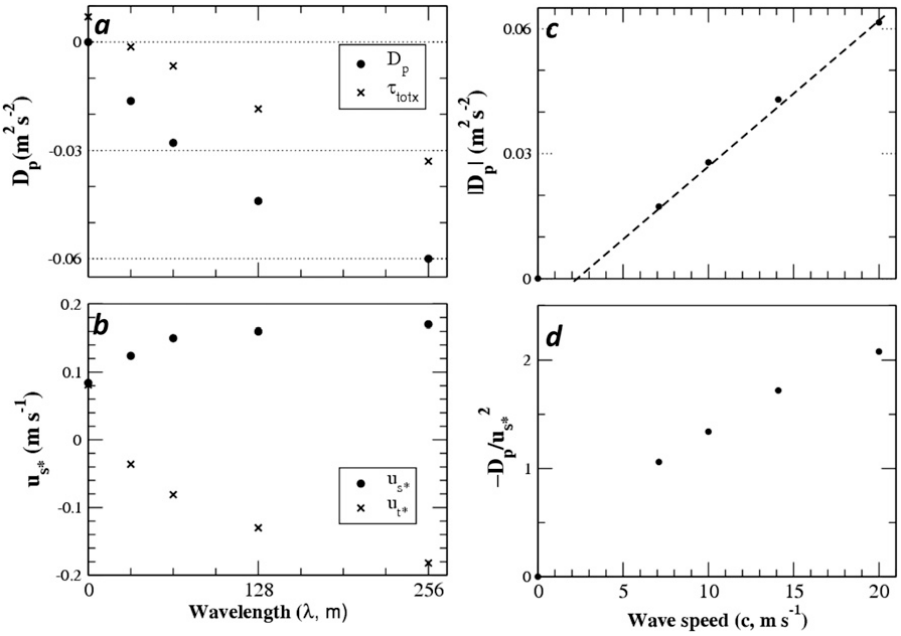

FIG. 1. Variation of (a) the wave form drag and total stress along the x direction and (b) the friction velocities u_{s*} and u_{t*}, with the swell wavelength derived from group A simulations with FLAT shown as $\lambda = 0$ just for comparison purpose. The wave form drag (c) as a function of wave speed and (d) as in (c), but normalized by u_{s*}^2.

and L256, respectively). L128 is also referred to as the control simulation (CTRL).

The corresponding flat surface simulation (FLAT) is included in Table 1 and Figs. 1–3 for comparison. With wave age c/U_g varying from 2.35 to 6.67, these simulations fall into the light-wind fast-wave regime, where we expect that swell has a significant impact on the WBL (e.g., Sullivan et al. 2008). The WBL is defined as the layer below half a wavelength in this study for simplicity. It is evident that the magnitude of both the form drag

$$D_p = \frac{1}{\lambda}\int_0^{\lambda} p^*(dz_b/dx)\,dx$$

where p^* denotes the perturbation pressure at the surface, normalized by air density and surface shear friction tends to increase with increasing wavelength (see Table 1 and Figs. 1a,b). The surface shear friction velocity, defined as $u_{s*}^2 = \tau_{sh}$ where τ_{sh} is the surface shear friction, is shown in Fig. 1 as a proxy for the total shear stress. It is worth noting that here u_{s*} is evaluated using winds at the first model level (i.e., at 1 m above the wave surface) instead of the 10-m level. Also shown in Fig. 1b is the friction velocity defined based on the total surface stress in the swell direction (i.e., the x direction), $u_{t*} = -\text{sign}(\tau_{totx})\sqrt{|\tau_{totx}|}$, where the x denotes the component along the x direction and $\tau_{totx} = \tau_{shx} + D_p$. Here we let u_{t*} be negative when the total stress is oriented along the geostrophic wind direction. The shear stress along the y direction is relatively small for most simulations and is therefore ignored. For $\lambda = 256$ m, the surface friction velocity is approximately twice as much

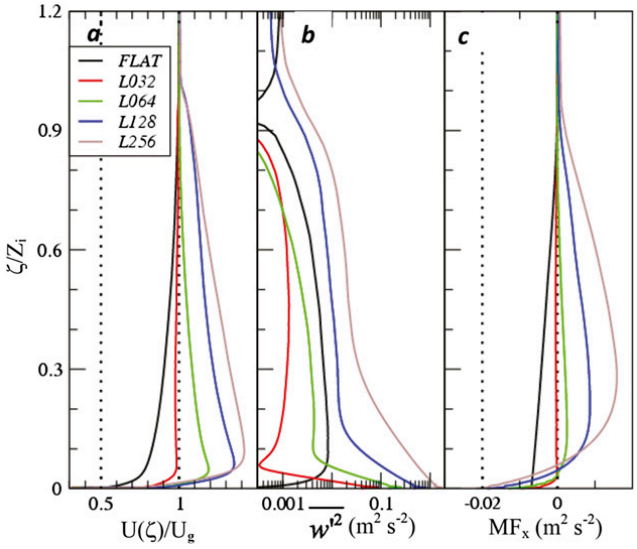

FIG. 2. Domain-averaged profiles of (a) normalized wind speed, (b) vertical velocity variance, and (c) momentum flux along the swell propagation direction (MF_x) valid at $T = 5$ h (averaged over ~15 min) derived from the group A simulations: FLAT (black), L032 (red), L064 (green), L128 (blue), and L256 (brown). The height above the wave surface is normalized by $Z_i = 300$ m.

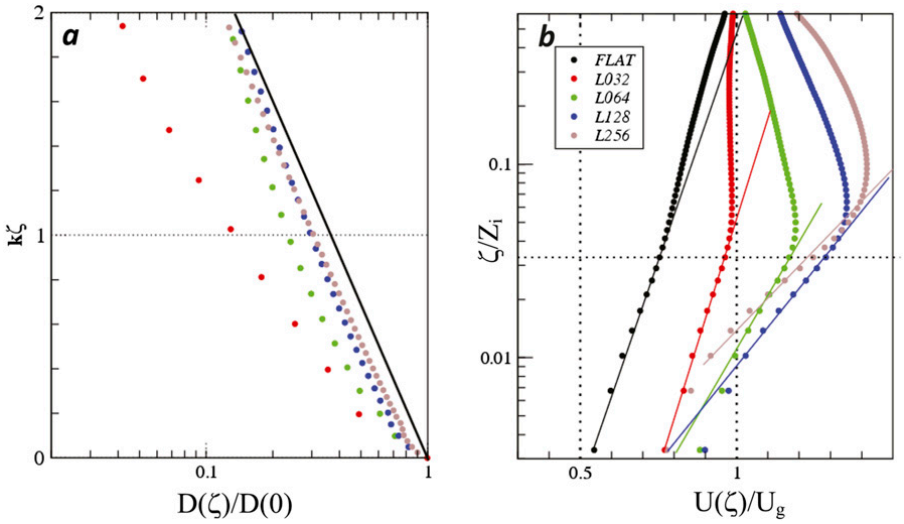

FIG. 3. (a) The normalized pressure stress $D(\zeta)/D(0)$ profiles from group A simulations on a log scale with the vertical distance nondimensionalized by multiplying by the wavenumber: FLAT (black), L032 (red), L064 (green), L128 (blue), and L256 (brown). The dark reference line corresponds to $e^{-k\zeta}$. (b) The normalized wind speed profiles on a log scale with the vertical distance normalized by $Z_i = 300$ m. The solid lines in (b) correspond to best-fit lines.

as the value derived from the reference flat surface simulation (Table 1), implying a quadruple increase of τ_{sh}. The large increase of u_{s*} with wavelength (or wave speed) is consistent with the enhancement of the wind speed and vertical wind shear in the WBL in the swell simulations.

For the swell simulations, the form drag is forward pointing (i.e., along the geostrophic wind direction), implying an upward momentum flux from the swell to the WBL. This is in qualitative agreement with previous studies of the swell effect in the light-wind fast-wave regime (e.g., Sullivan et al. 2008). Further inspection of the results in Table 1 suggests that, for fixed wave slope $s = 0.1$, the form drag increases nearly linearly with the swell phase speed, approximately as $D_p \approx 0.003(c - U_s)$, where $U_s = 2.1\,\mathrm{m\,s^{-1}}$ (see the dashed line in Fig. 1c), implying that more momentum is transferred from faster-propagating swell into the WBL. The form drag normalized by the friction velocity squared increases with the wave speed as well (Fig. 1d), implying that the increase of the turbulence stress is slower than that of the form drag over the range of parameters examined. The best-fit quadratic polynomial describing the variation of D_p as a function of u_{s*} is $D_p = 8.12(u_{s*} - u_{s*,0})^2$, where $u_{s*,0} = 0.084\,\mathrm{m\,s^{-1}}$ is the friction velocity obtained from the flat surface simulation. The total x-direction surface stress τ_{totx} is virtually zero for L032 and becomes negative for swell with a longer wavelength (Fig. 1a).

The vertical profiles of horizontally and temporally averaged wind speed, vertical velocity variance, and momentum flux obtained from these simulations are shown in Fig. 2. Compared to FLAT, it is evident that the wind speed throughout the boundary layer is modified by swell (Fig. 2a). FLAT produces a typical boundary layer wind speed profile with the wind speed following the log law to a good approximation in the surface layer and gradually tending to the geostrophic wind speed aloft. In the swell experiments, a super-geostrophic jet is evident in the three simulations with longer wavelength (i.e., L064, L128, and L256) and the jet strength tends to increase with the wavelength (Fig. 2a and Table 1). This is consistent with the increase of $|\tau_{totx}|$ with the swell wavelength (Fig. 1a), implying the dependence of the jet intensity on the negative surface stress. The level of the wind maximum z_m shows a marked increase with the wavelength. However, this increase is slower than proportional to the wavelength (i.e., kz_m decreases with increasing λ, Table 1). It is interesting that, as τ_{totx} is virtually zero in L032, the wind profile shows a marginal jet with a maximum wind speed near U_g, suggesting that $\tau_{totx} < 0$ is likely a necessary condition for the formation of a wave-driven super-geostrophic jet. It is also worth noting that, for L064, L128, and L256, the v wind is negative (not shown), in contrast to a positive v wind in FLAT or in a typical Ekman boundary layer.

In Fig. 2b, the vertical velocity variance profiles are shown as a proxy for turbulence kinetic energy (TKE). For the FLAT simulation, the variation of $\overline{w'^2}$ with height exhibits a typical TKE profile in a nonconvective atmospheric boundary layer over a flat surface. In contrast, $\overline{w'^2}$ from the swell simulations is characterized by a

maximum at the surface with a significant wave-induced contribution, which decays with the vertical distance from the wavy surface. Further inspection indicates that $\log[\overline{w'^2}(\zeta)]$ decreases nearly linearly with $k\zeta$ for $0 < k\zeta < 2$, with an average slope around -0.8 (i.e., $\overline{w'^2} \sim e^{-\alpha_w k\zeta}$ in the WBL where the coefficient $\alpha_w = 0.8$). For L032 and L064, $\overline{w'^2}$ exhibits a well-defined minimum near the top of the WBL, above which direct wave contribution diminishes. For L032, the wind speed is nearly uniform above the WBL top, where the turbulence virtually disappears (i.e., $\overline{w'^2} \sim 0$). For the other swell simulations, the turbulence remains active above the WBL in accordance with the negative vertical wind shear. Compared with FLAT, noticeably stronger entrainment occurs near the boundary layer top (i.e., larger negative buoyancy flux; not shown) for L128 and L256 associated with the more intense jet and hence shear-enhanced turbulence aloft, which leads to about a 20% increase in the boundary layer depth.

The horizontally averaged x-momentum equation can be written as in Sullivan et al. (2014):

$$\frac{\partial}{\partial t}\left\langle \frac{\overline{u}}{J} \right\rangle = -\frac{\partial}{\partial \zeta}\left\langle \overline{u}(W - z_t) + \tau_{11}\frac{\zeta_x}{J} + \tau_{23}\frac{\zeta_z}{J} \right\rangle - \frac{\partial}{\partial \zeta}\left\langle p^*\frac{\zeta_x}{J} \right\rangle + f\left\langle \frac{\overline{v}}{J} \right\rangle, \quad (1)$$

where the angle brackets and overbars denote time and horizontal averaging, respectively, J is the Jacobian of the grid transformation, W is the contravariant flux velocity normal to a ζ surface, and τ_{11} and τ_{13} denote the SGS momentum fluxes. As the Coriolis term is relatively small in this study, Eq. (1) suggests that the mean wind profile is largely controlled by the vertical divergence of the momentum flux, including contributions from resolved momentum flux, $\langle \overline{u}(W - z_t)\rangle$, and SGS fluxes, $\langle \tau_{11}(\zeta_x/J) + \tau_{23}(\zeta_z/J)\rangle$, and the pressure stress, $D(z) = (\partial/\partial\zeta)\langle p^*(\zeta_x/J)\rangle$ (i.e., the pressure–wave slope correlation). For the monochromatic waves used in this study, $D(z) = (-1/\lambda)\int_0^\lambda p^* z_\zeta \, dx$, where z_ζ denotes the slope of the ζ-coordinate lines in physical space.

The horizontally averaged x-direction momentum fluxes (denoted as MF_x) shown in Fig. 2c, are the sum of the resolved and SGS fluxes derived from the group A simulations. The SGS flux is characterized by a negative maximum at the surface and rapidly decreases to virtually zero near the WBL top. Above the WBL, the momentum flux is dominated by the resolved turbulence contribution. For FLAT, MF_x is negative with its magnitude linearly decreasing with height toward zero, in accordance with generally downward momentum mixing as in a typical atmospheric boundary layer over a homogenous flat surface. For L032, MF_x is negative in the WBL and becomes virtually zero aloft, consistent with the extremely weak turbulence above the WBL. For L064, L128, and L256, MF_x is negative in the WBL and becomes positive aloft, implying upward momentum mixing in accordance with the negative wind shear above the wind maximum. It is noteworthy that for L064, L128, and L256, the total momentum flux (i.e., $\mathrm{MF}_x + D$) is nonnegative throughout the boundary layer, implying that the total momentum is actually transferred upward and the swell serves as a momentum source under light-wind swell-dominated conditions. This is in contrast to a typical boundary layer over a flat surface, in which the momentum is mixed downward from the free atmosphere and removed at the surface by shear stress.

A couple of issues arise from this group of simulations that deserve further discussion. First, the vertical divergence of the pressure stress plays an important role in the momentum balance in the lower portion of the boundary layer, especially within the WBL. Accordingly, how fast the pressure stress decays with the vertical distance is of critical importance to the dynamics in the WBL, such as the formation of the wave-driven jet. In analytical WBL models, the wave stress is often assumed to decay exponentially with distance from the sea surface (i.e., $\propto e^{-\zeta/L_d}$) and the characteristic vertical length scale L_d varies between studies (e.g., Hanley and Belcher 2008; Semedo et al. 2009). To shed light on this issue, the normalized horizontally averaged pressure stress from the swell simulations is plotted on a log scale as a function of $k\zeta$ in Fig. 3a. In general, the pressure stress exhibits an approximate exponential decay with vertical distance for $0 < k\zeta < 2$, except for the profile from L064, which decays faster for $0 < k\zeta < 1$ and slower for $1 < k\zeta < 2$. Letting $D \sim e^{-\alpha_p k\zeta}$ [i.e., $L_d = 1/(\alpha_p k)$], the average α_p for $0 < k\zeta < 1$, estimated from Fig. 3a, is listed in Table 1. In general, D decays faster with vertical distance than in potential flow (i.e., $\alpha_p = 1$). Theoretically (e.g., Cohen and Belcher 1999), the vertical decay of the wave-induced perturbations is controlled by the vertical stratification (i.e., neutral in this study) and the vertical gradient of the wind (i.e., dU/dz and d^2U/dz^2; e.g., Jenkins 1993). The relatively large variation of α_p between simulations is likely attributed to the difference in the wind profiles, which are in turn partially controlled by the vertical divergence of pressure stress.

Second, while Monin–Obukhov similarity theory (MOST) is still widely used in mesoscale models for diagnosing the surface stress, its validity over swell has been questioned in a number of studies (e.g., Drennan et al. 1999; Janssen 2004; Sullivan et al. 2008). The surface layer simulated in this study is neutrally stratified and according to MOST, the wind speed should follow

the log law in the surface layer (Tennekes 1973). It is evident that the wind speed profiles from FLAT and L032 follow a log law to a good approximation up to ~15 m (Fig. 3b), although the WBL wind in L032 is stronger and the best-fit line has a steeper slope than in FLAT. For longer wavelengths, the wind speed profile in the near surface layer appears to deviate from a log law. For L064, L128, and L256, it is evident that the simulated profile concaves away from the corresponding line connecting $\zeta = 1$ and 10 m, suggesting a breakdown of the log law. However, the wind speed profiles between 3–12 m for L064 and 3–15 m for L128 and L256 approximately follow a logarithmic variation. The extrapolation of the best-fit lines (thin lines in Fig. 3b) to $\zeta = 1$ m yields substantially lower wind speed than the corresponding simulated wind speed, suggesting that the forward-pointing form drag has increased the wind speed near the surface.

For each simulation, the friction velocity and surface roughness length (denoted as u_{p*} and $z_{p,0}$ where p stands for parameters derived using the profile method) can be obtained from the best-fit lines in Fig. 3b using $U(z) = (u_{p*}/\kappa)\ln(z/z_{p,0})$, along with the drag coefficient $C_{d,10,p} = (u_{p*}/U_{10})^2$. Also included in Table 1 are the drag coefficients obtained using the surface shear stress, $C_{d,10,s} = (u_{s*}/U_{10})^2$, and total x-direction stress, $C_{d,10,t} = \tau_{totx}/U_{10}^2$, for comparison. It is interesting to compare the three drag coefficients. While they are virtually equal to each other for FLAT, they can be strikingly different for the simulations with swell (Table 1). Physically, u_{p*}^2 represents the stress needed at the surface to maintain the enhanced wind shear in the log-law layer. Hence, there is no direct relationship between u_{p*}^2 and the actual air–sea momentum exchange. The total air–sea momentum exchange (i.e., τ_{totx}) is in fact significantly less than u_{p*}^2 in all simulations except for FLAT (Fig. 4). The total stress based definition is physically more consistent, considering that (i) τ_{totx} is nearly constant with height in the surface layer (Sullivan et al. 2014), (ii) τ_{totx} is one of the standard variables directly measured in the field, and (iii) $C_{d,10,t}U_{10}^2$ gives the total air–sea momentum exchange.

The large discrepancy between $C_{d,10,t}$ and $C_{d,10,p}$ (or between u_{p*}^2 and τ_{totx}) for swell simulations is largely attributed to the pressure stress and casts doubt upon the validity of MOST over ocean swell in light-wind conditions. The pressure stress distinguishes itself from typical turbulence stress in following aspects: (i) it can be positive or negative in the surface layer while the latter is always positive; (ii) unlike the latter, there is no proportional relationship between the pressure stress and the vertical wind shear; and (iii) pressure stress introduces a new vertical length scale L_d, which is largely determined by the swell wavelength. The latter two features violate the basic hypotheses that MOST is based on. Therefore, when the contribution from the pressure stress dominates the shear stress, MOST likely becomes improper for describing the surface layer and air–sea momentum exchange, even when the observed or simulated wind profile follows the log-law reasonably well under neutral conditions.

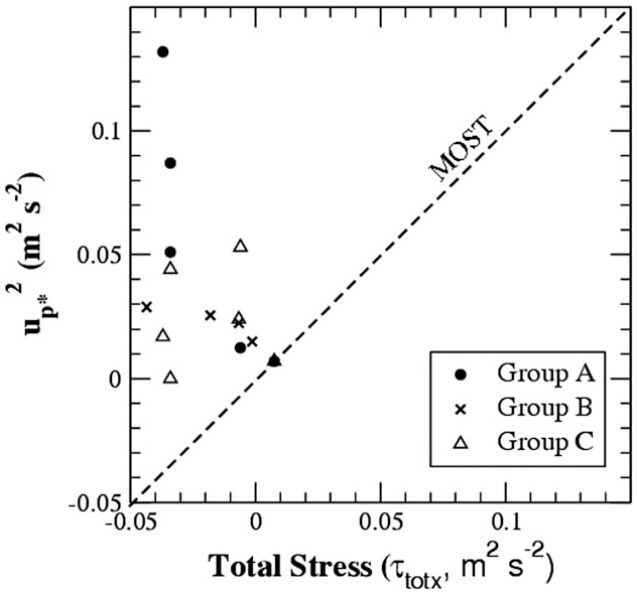

FIG. 4. The surface stress derived from the profile method (i.e., u_{p*}^2) plotted against the total surface stress (τ_{totx}) for the three groups of LESs: A, B, and C. The dashed line corresponds to $\tau_{totx} = u_{p*}^2$.

b. *Wave slope*

To examine how the air–sea momentum exchange and the wave-driven jet vary with the swell slope, we have conducted a group of simulations (i.e., group B), using the same model configuration as in CTRL but with wave slope $s = ak = 0.05$, 0.1, 0.2, 0.3, and 0.4, respectively. These simulations are referred to as S05, S10 (i.e., CTRL), S20, S30, and S40, and the model results are summarized in Table 2 and Figs. 5–7. Although waves with $s = 0.3$ or larger are highly nonlinear, they are not necessarily breaking. Breaking of ocean waves may significantly complicate air–sea momentum exchange and is not considered in this study. In addition, no airflow separation is observed in these simulations.

According to Figs. 5a,b, both the form drag and the surface friction velocity appear to increase linearly with the wave slope. The linear increase of the form drag with wave slope is in contrast to linear theory, which predicts that the form drag is proportional to the wave slope squared (e.g., Belcher and Hunt 1993). This apparent

TABLE 2. List of simulations and derived parameters around $T = 5$ h from group B simulations with the control (i.e., S10) highlighted in bold. The parameters are identical to those in Table 1, except that the wavelength ($\lambda = 128$ m) is not included.

Expt	c/U_g	u_{s*} (m s^{-1})	u_{p*} (m s^{-1})	α_p	U_{10} (m s^{-1})	U_m (m s^{-1})	$kz_{\max}$	$C_{d,10,s}$ ($\times 10^{-3}$)	$C_{d,10,t}$ ($\times 10^{-3}$)	$C_{d,10,p}$ ($\times 10^{-3}$)
FLAT	N/A	0.084	0.089	—	2.26	3.00	—	1.4	1.4	1.5
S05	4.71	0.112	0.23	1.1	3.10	3.47	1.01	1.3	−0.63	5.5
S10	**4.71**	**0.160**	**0.208**	**1.05**	**3.85**	**4.00**	**0.94**	**1.7**	**−1.2**	**2.9**
S20	4.71	0.226	0.21	0.82	4.22	4.42	0.94	2.9	−1.9	2.5
S30	4.71	0.295	0.21	0.74	4.79	5.00	0.94	3.8	−1.5	1.9
S40	4.71	0.363	0.13	0.69	5.15	5.25	0.87	5.0	−1.4	0.64

discrepancy is likely due to the breakdown of the linear theory assumptions over steep waves. Also included in Figs. 5a,b are the best-fit lines, corresponding to $D_p = 0.37(ak)$ and $u_{s*} - u_{s*,0} \approx 0.70(ak)$, respectively. The increase of the friction velocity with the swell slope is consistent with the increase of the wind speed in the WBL, suggesting that the enhanced wind speed in the WBL in turn regulates the form drag and shear stress at the surface. This nonlinear dynamic coupling between the airflow and the underlying wave surface is not taken into account in any linear theory. The total stress along the x direction decreases sharply with the increasing wave slope for $s < 0.2$.

The horizontally averaged profiles for this group of simulations are shown in Fig. 6. A wave-driven jet is present in all the swell simulations, being consistent with the negative τ_{totx} in these simulations. The simulated wind speed maximum is 3.1 m s^{-1} for S05, slightly above U_g and becomes 5.25 m s^{-1} for S40, substantially stronger than U_g (Fig. 6a). The height of the wind maximum tends to decrease with the increasing wave slope, likely owing to the increase in form drag (see further discussion in section 4). Similar to the group A simulations, in the presence of swell, the $\overline{w'^2}$ profile is characterized by a surface maximum directly generated by wave forcing, which decays exponentially with the altitude in the WBL (Fig. 6b). For swell with a slope $s = 0.2$ or steeper, $\overline{w'^2}$ decreases more slowly with height between the WBL top and ~$0.8Z_i$, in accordance with the linear wind shear above the jet. If we define the boundary layer top based on the TKE, the boundary layer is noticeably deeper over steeper swell. The momentum flux profiles for the swell simulations in group B are qualitatively similar. The magnitude of the negative maximum near the surface increases substantially with swell slope, implying stronger downward momentum mixing in the WBL over steeper swell. The altitude where the momentum flux changes signs becomes progressively higher, and the positive maximum aloft increases with slope for $s < 0.2$ and decreases with further increase of the slope, likely because the negative shear above the wind maximum is distributed over a deeper layer for S30 and S40, in accordance with a deeper boundary layer and stronger turbulence aloft.

In the WBL, the estimated e-folding decay distance of the pressure stress is larger over steeper swell (Fig. 7a, Table 2), and the pressure stress decreases substantially slower with height for $s = 0.2$ and steeper. Figure 7b shows that except for FLAT and S04, the simulated wind speed profiles clearly concave away

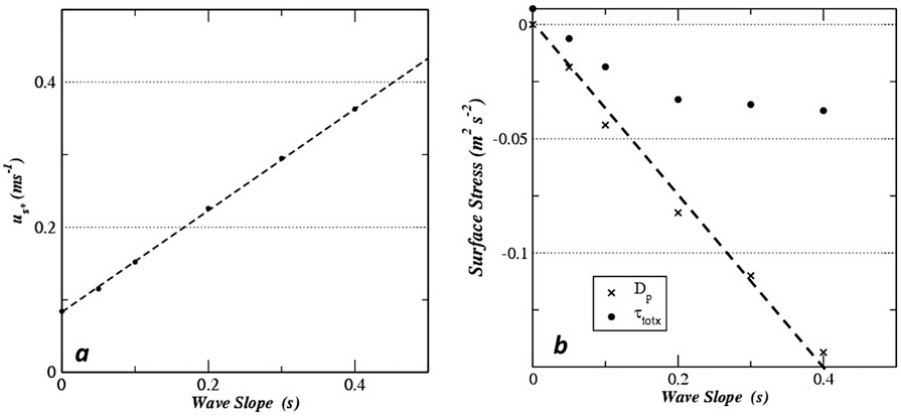

FIG. 5. (a) Variation of the shear friction velocity with the wave slope derived from group B simulations valid at 5 h. (b) The corresponding wave form drag D_p and total x-direction stress τ_{totx}. The dashed lines correspond to the best-fit curves.

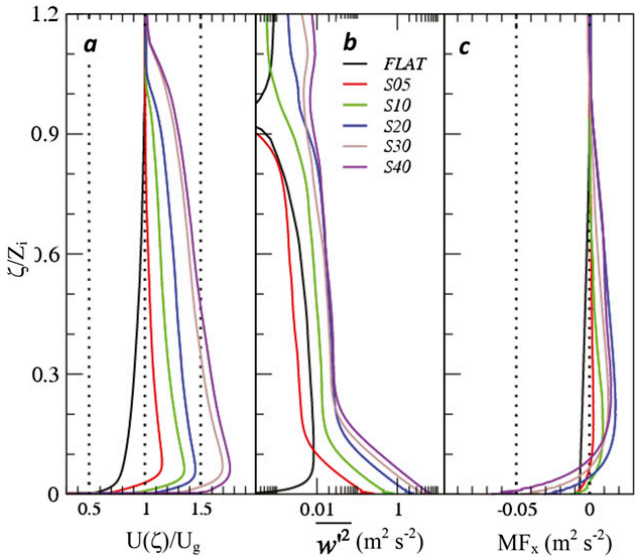

FIG. 6. As in Fig. 2, but for simulation group B: FLAT (black), S05 (red), S10 (green), S20 (blue), S30 (brown), and S40 (purple).

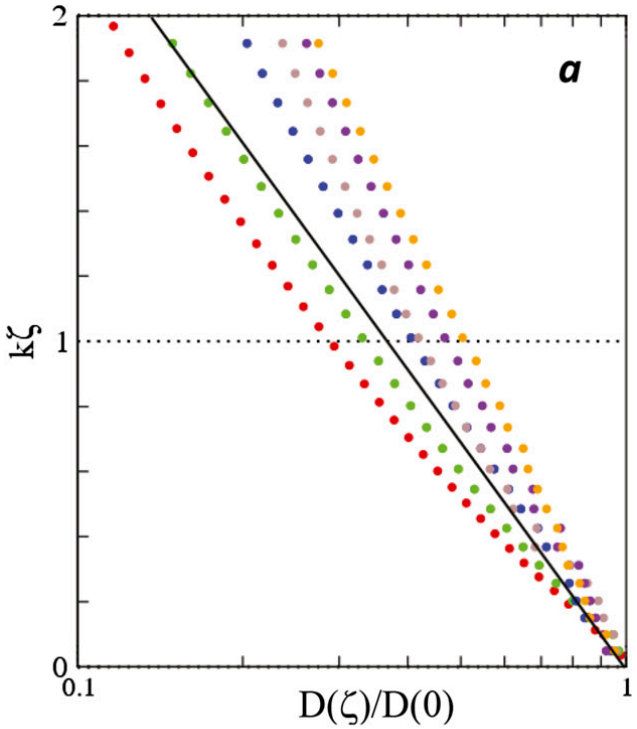

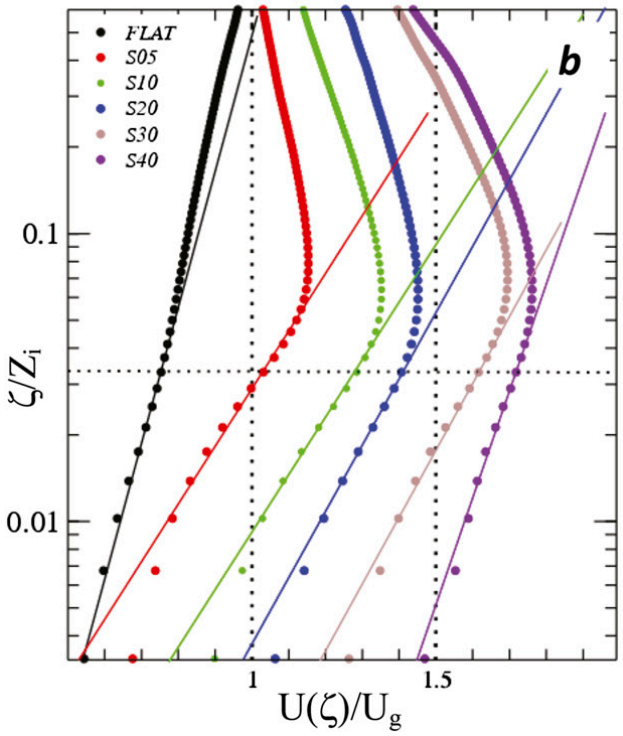

FIG. 7. As in Fig. 3, but for group B simulations: FLAT (black), S05 (red), S10 (green), S20 (blue), S30 (brown), and S40 (purple).

from the best-fit line between $\zeta = 1$ and 10 m (Fig. 7b), implying that they do not strictly follow the log law. However, for S05, S10, S20, and S30, a nearly linear segment in the wind speed exists between 3 and 12 m when plotted on a logarithmic scale. The wind speed at 1 m extrapolated from the best-fit lines for these simulations is weaker than the simulated one, and the difference becomes consistently smaller over steeper swell. For S40, the wind speed follows the log law reasonably well between 1–15 m (see the purple line in Fig. 7a). The friction velocity, surface roughness length, and drag coefficient (i.e., u_{p*} and $C_{d,10,p}$) derived from these best-fit lines are included in Table 2. While the surface shear stress and 10-m wind consistently increase with s, u_{p*} is comparable for S05, S10, S20, and S30 and becomes substantially smaller in S40. The drag coefficient $C_{d,10,p}$, is the largest for S05 and decreases rapidly for a larger s, implying that the sea surface becomes ''smoother'' over steeper wind-following swell. Again, the fairly large difference between the total stress based drag coefficients $C_{d,10,t}$ and $C_{d,10,p}$ suggests that the MOST is invalid here, regardless of whether the simulated wind speed follows the log law in the surface layer.

c. *Wind speed*

According to previous studies, the swell impact is more (less) significant in the presence of wind-opposing (following) swell and is more important under lighter wind conditions (i.e., $U_{10}/c < 1$) for wind-following swell. To further explore the wind speed dependence of the swell impact, we have conducted six additional

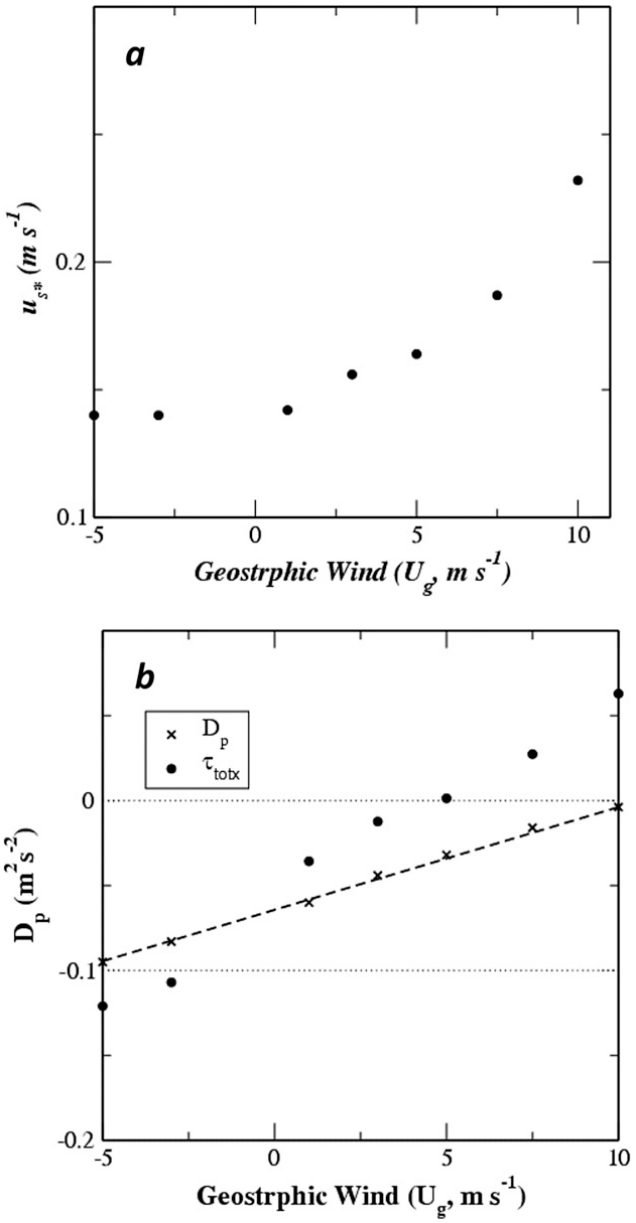

FIG. 8. As in Fig. 5, but for the geostrophic wind derived from group C simulations.

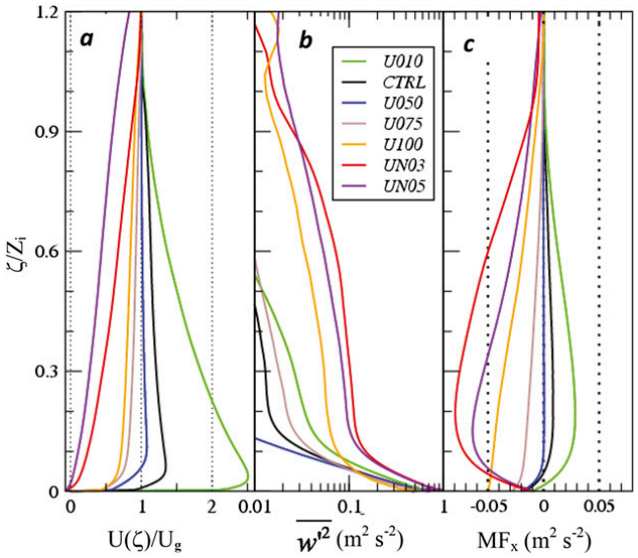

FIG. 9. As in Figs. 2 and 6, but derived from simulations in group C: U010 (green), CTRL (black), U050 (blue), U075 (brown), U100 (orange), UN03 (red), and UN05 (purple).

simulations with the same model configuration as in CTRL except that $U_g = -5, -3, 1, 5, 7.5$, and $10\,\mathrm{m\,s^{-1}}$ (referred to as UN50, UN30, U010, U050, U075, and U100, respectively; here N denotes $U_g < 0$, implying that the swell is wind opposing). With the maximum U_g/c less than 0.71, these simulations are still in the fast-wave regime and no complexity associated with the critical level (i.e., the level the wind speed matches the wave speed) dynamics is involved.

As shown in Fig. 8, the magnitude of the form drag is much larger in the presence of wind-opposing swell (i.e., $U_g < 0$) and decreases linearly with the increase of the geostrophic wind. The best linear-fit line corresponds to $D_p = 0.006\,215\,7(U_g - U_{g,0})$, where $U_{g,0} = 10.3\,\mathrm{m\,s^{-1}}$ (or $U_{g,0}/c \sim 0.72$). The form drag reverses sign when U_g exceeds $U_{g,0}$, which is in qualitative agreement with the DNSs of the Couette flow over a monochromatic wave reported in Sullivan and McWilliams (2002). The surface friction velocity is nearly constant when U_g increases from -5 to $1\,\mathrm{m\,s^{-1}}$, in accordance with the relatively weak winds near the surface. The total stress along the x direction also increases linearly with U_g as $\tau_{\mathrm{totx}} = 0.0125(U_g - U_{g,1})$, which changes sign near $U_{g,1} \sim 5.1\,\mathrm{m\,s^{-1}}$, or in terms of an inverse wave age, $U_{g,1}/c \sim 0.36$. Hence, for $U_{g,1} < U < U_{g,0}$, τ_{totx} becomes positive, although the form drag is still negative. The sign reversal of the total stress was found in field experiments as well except that the threshold inverse wave age is smaller (i.e., $U_g/c \sim 0.15$–0.2). Presumably the two threshold wind speeds are functions of swell properties or, in general, the sea state.

A wave-driven wind jet appears in the simulations with $U_g \le U_{g,1}$ and $\tau_{\mathrm{totx}} < 0$ (Fig. 9a). The normalized jet strength increases with decreasing wind speed, implying that the swell impact is generally more significant under lighter wind conditions. The maximum wind speed level appears to be higher for a larger U_g. With wind-opposing swell, the form drag is positive (i.e., same sign as the shear stress) and substantially larger in magnitude than with wind-following swell, and consequently, the wind speed in the lower to middle boundary layer is much reduced. In the WBL, the wind-opposing swell produces larger vertical velocity

variance (Fig. 9b). Above the WBL, the wind-opposing swell also generates significantly stronger turbulence and accordingly the boundary layer is deeper in UN30 and UN50. For U050, the normalized maximum wind speed is only slightly above unity, as τ_{totx} is close to zero. Consequently, the turbulence is extremely weak and the boundary layer is shallow (~40 m). For U010, U030, and U075, the turbulence is largely confined to the lowest 150 m owing to the relatively weak vertical wind shear aloft. The turbulence is substantially stronger and the boundary layer is much deeper (~300 m) in U100, UN30, and UN50, associated with stronger vertical wind shear. The MF_x profiles for the group C simulations can be separated into three categories. For U010, U030 (i.e., CTRL), and U050, MF_x is negative below and positive aloft, being consistent with the presence of a wave-driven wind jet (Fig. 9c). For U075 and U100, MF_x is negative throughout the whole boundary layer with the magnitude linearly decreasing with the altitude, qualitatively resembling FLAT. For the two wind-opposing swell simulations, MF_x is characterized by a negative maximum located near the WBL top. Decelerated by both the shear stress and form drag, the WBL flow is extremely weak in these simulations, and accordingly the downward mixing of momentum is weak.

For simulations with $U_g < 5\,m\,s^{-1}$, the pressure stress seems to exhibit an exponential decay in the WBL with the e-folding decay distance L_d varying with U_g. The decay distance is larger in UN30 and UN50 (Fig. 10a and Table 3) and becomes consistently shorter with increasing U_g with wind-following swell. For $U_g = 3\,m\,s^{-1}$ or larger, the drag profile clearly deviates from an exponential decay; the drag decays more rapidly for $k\zeta < 1$ and substantially slower for $1 < k\zeta < 2$.

The wind profiles from U010, UN3, UN5, U075, and U100 follow a log law reasonably well between 1 and ~10 m. Specifically, the shallowest log-law layer occurs in U010 (~9 m) and the deepest in UN5 (~30 m). The wind profiles of U030 and U050 concave away from the reference lines between 1–10 m, and yet they approximately follow a log law between 3 and ~12 m. Accordingly, u_{p*} and $C_{d,10,p}$ can be estimated for these best-fit lines (Table 3). For the wind-following swell simulations, $C_{d,10,p}$ is substantially larger than $C_{d,10,t}$.

Surprisingly, for UN3 and UN5, although the wind profile follows the log law nicely up to $\zeta/Z_i \sim 0.1$ (i.e., 30 m above the wave surface), $C_{d,10,p}$ is significantly larger than $C_{d,10,t}$, suggesting that MOST may not be applicable. For these two simulations, the turbulence stress and the form drag share the same sign, both of which tend to decelerate the WBL flow.

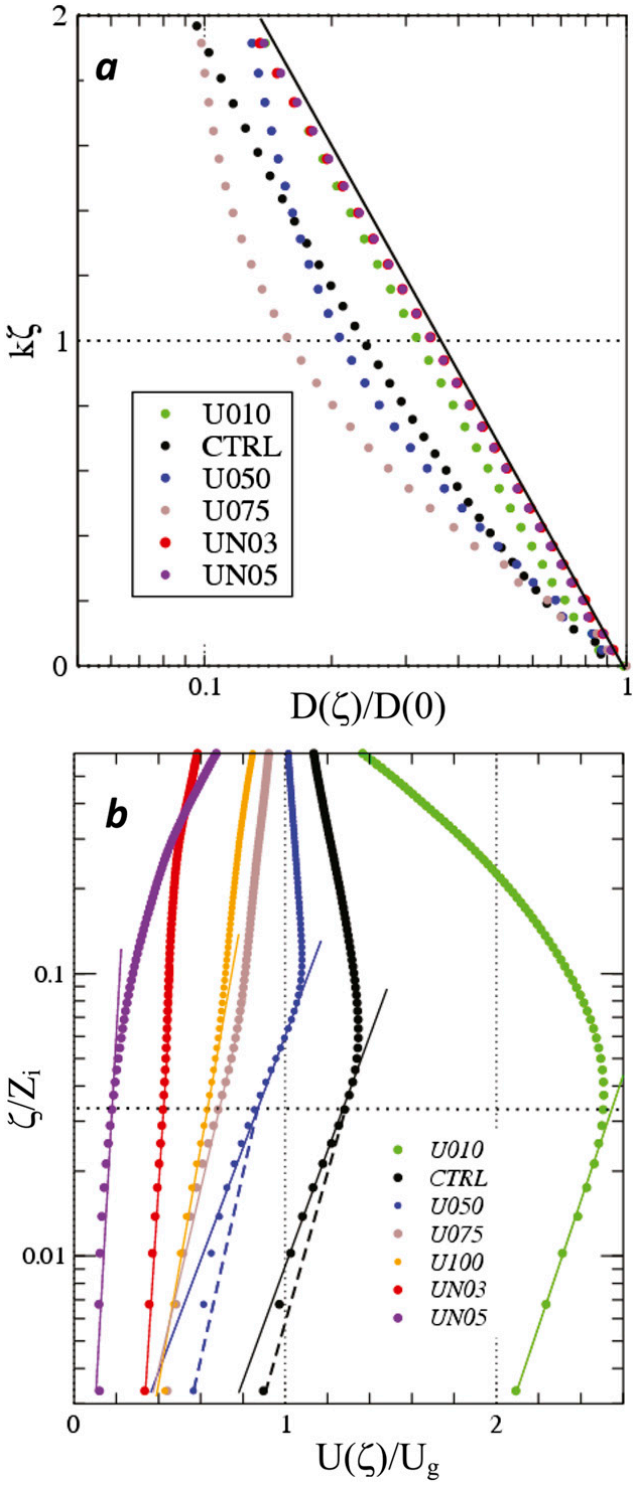

FIG. 10. As in Figs. 3 and 7, but for group C simulations: U010 (green), CTRL (black), U050 (blue), U075 (brown), U100 (orange), UN03 (red), and UN05 (purple). The two dashed lines in (b) connect $\zeta = 1$ and 10 m for CTRL (black) and U050 (blue), respectively, for comparison.

TABLE 3. List of simulations and derived parameters around $T = 5$ h from group C simulations. The control simulation is highlighted in bold. The parameters are identical to those in Table 2.

Expt	c/U_g	u_{s*} (m s^{-1})	u_{p*} (m s^{-1})	α_p	U_{10} (m s^{-1})	U_m (m s^{-1})	$kz_{\max}$	$C_{d,10,s}$ ($\times 10^{-3}$)	$C_{d,10,t}$ ($\times 10^{-3}$)	$C_{d,10,p}$ ($\times 10^{-3}$)
U010	14.1	0.141	0.080	1.15	2.50	2.51	0.54	3.2	−6.5	1.0
U030	**4.71**	**0.160**	0.208	**1.28**	**3.85**	**4.00**	**0.94**	**1.7**	**−1.2**	**2.9**
U050	2.82	0.164	0.320	1.61	4.27	5.40	1.65	1.5	−0.28	5.6
U075	1.88	0.187	0.350	1.85	5.12	—	—	1.3	0.70	4.7
U100	1.41	0.240	0.300	2.05	6.30	—	—	1.4	1.4	2.3
UN30	4.71	0.140	0.034	1.05	0.555	—	—	64	292	3.8
UN50	2.82	0.144	0.078	1.05	2.14	—	—	4.5	22	1.3

4. Discussion

These LESs cover a relatively large parameter space and shed light on a number of issues that are of critical importance to the understanding of air–sea interaction over swell-dominated ocean areas, including what determines the characteristics of the wave-driven wind jet, how the form drag varies with the swell property and winds, and how the turbulence and wind profiles respond to the swell forcing. These issues are further discussed in this section assisted by an analytical one-dimensional WBL model.

a. *Characteristics of wave-driven wind jet and wind profiles in the surface layer*

Previous studies suggested that one-dimensional boundary layer or surface layer models can be helpful in assisting the interpretation of the observed or simulated wave-driven wind jet (e.g., Chalikov and Belevich 1993; Hanley and Belcher 2008; Semedo et al. 2009). To understand the formation condition and dependence of wave-driven jets on the control parameters examined, we adopt the simple one-dimensional WBL model described in Semedo et al. (2009, hereafter S09). In an equilibrium WBL, assuming that the Coriolis term is negligible, the horizontally integrated total stress is nearly constant with height; that is,

$$\frac{d\tau_{\text{totx}}}{dz} = \frac{d(\tau_{\text{wave}} + \tau_{\text{turb}})}{dz} = 0, \tag{2}$$

where the wave stress is assumed to decay exponentially with z,

$$\tau_{\text{wave}} = D_p e^{-k'z}, \tag{3}$$

and D_p is the wave stress at the surface. Here $k' = 2\pi/L_d$ and L_d is the vertical e-folding decay distance of the wave stress. In this study, we let $k' = \alpha_p k$, where the coefficient α_p is listed in the tables. We further assume that the turbulence stress is proportional to the mean wind shear; that is,

$$\tau_{\text{turb}} = K_m \frac{dU}{dz}, \tag{4}$$

where the turbulent eddy viscosity K_m can be written as $K_m = \kappa z u_*$ in the WBL. Using (2)–(4), we have

$$\kappa u_* U(z) = \tau_{\text{totx}} \ln\left(\frac{z}{z_0}\right) - D_p \int_{z_0}^{z} \frac{e^{-\alpha_p kz}}{z} dz. \tag{5}$$

A wave-driven jet, if it exists, is located at a level where $dU/dz = 0$, which yields

$$kz_{\max} = -\frac{1}{2\alpha_p} \ln(1+\beta), \tag{6}$$

where $\beta = \tau_{\text{sh}}/D_p$ is the ratio between the surface shear stress and form drag. According to (6), a wave-driven wind jet only exists when the magnitude of the negative form drag is larger than the shear stress (i.e., $0 > \beta > -1$). The wind maximum level is determined by the e-folding decay distance of the form drag and the ratio between τ_{sh} and D_p. As an example, for $\beta = -0.25$, -0.5, -0.75, and -0.95, we have $\alpha_p kz_{\max} = 0.144$, 0.34, 0.69, and 1.5, and for $k = 2\pi/128\,\text{m}^{-1}$ and $\alpha_p = 1$, (5) yields $z_{\max} =$ 2.93, 6.90, 14.0, and 30.4 m, respectively. The nondimensional wind jet levels derived from LESs are plotted in Fig. 11 as a function of $-\beta$ using $k' = \alpha_p k$ with α_p values from Tables 1–3. The bold curve, corresponding to (6) with $\alpha_p = 1$, is included for comparison. In general, the LES results are in qualitative agreement with the prediction from (6), suggesting the critical role the ratio between shear stress and form drag plays in determining the wind maximum level.

For a thin layer above the wave surface satisfying $z_0 \ll z$ and $kz \ll 1$, we have $e^{-\alpha_p kz} \approx 1 - \alpha_p kz$, and (5) can be approximated as

$$\kappa u_* U(z) = \tau_{\text{totx}} \ln\left(\frac{z}{z_0}\right) - D_p \ln\left(\frac{z}{z_0}\right) + D_p \alpha_p kz. \tag{7}$$

The ratio between the third and second terms illustrates how far away the wind profile departs from a log

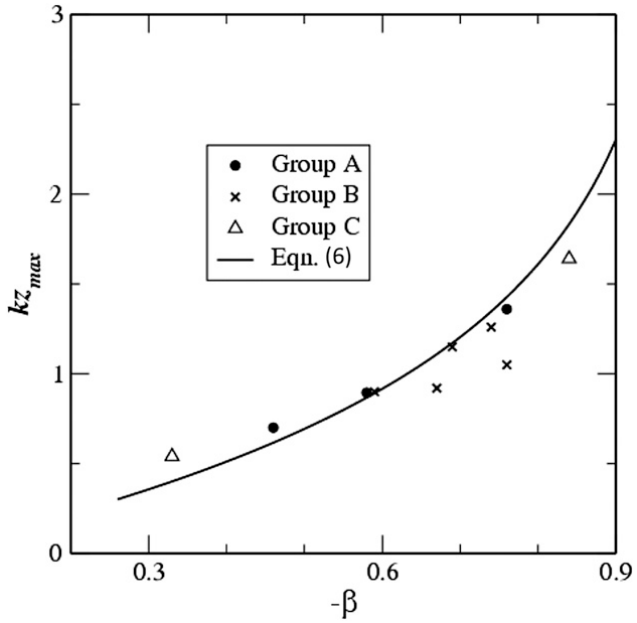

FIG. 11. Nondimensional wind maximum level vs β the ratio between the shear stress and wave drag from simulations that produce wave-driven jets in groups A, B, and C. The solid curve corresponds to Eq. (6) with $\alpha_p = 1$.

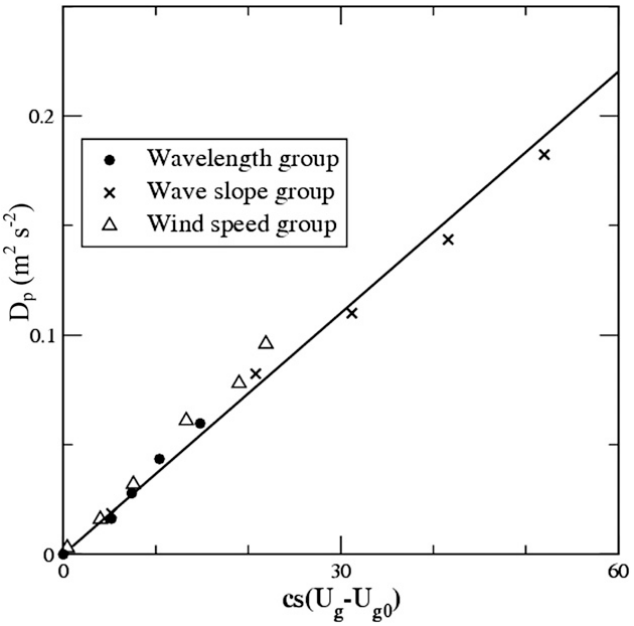

FIG. 12. The wave form drag from three groups—wavelength, slope, and speed—vs $cs(U_g - U_{g,0})$. The best-fit curve corresponding to $D_p = 0.003\,67cs(U_g - U_{g,0})$ with $U_{g,0} = 10.3\,\mathrm{m\,s^{-1}}$ included for comparison.

law. For example, letting $z = 5\,\mathrm{m}$, $z_0 = 0.0002\,\mathrm{m}$, $k = 2\pi/128\,\mathrm{m}^{-1}$, and $\alpha_p = 1$, we have $\alpha_p kz\,\ln^{-1}(z/z_0) = (10\pi/128)\ln^{-1}(25\,000) \sim 0.024$. In this example, the last term on the right-hand side is less than 3% of the second term and, therefore, negligible. Accordingly, the wind profile in the vicinity of $z = 5\,\mathrm{m}$ follows a log law reasonably well. This simple exercise provides a plausible explanation of the apparent contradiction between the existence of a log-law layer in the simulated wind profiles and the clear violation of the MOST assumptions.

b. *Wave form drag*

Wave form drag plays an instrumental role in the formation of wave-driven jets and in forcing the growth (or decay) of the swell itself. According to the simulations presented in this study, the dependence of the form drag on the wave speed, wave slope, and geostrophic winds can be written as

$$D_p = \gamma c(ak)(U_g - U_{g,0}), \tag{8}$$

where the threshold wind speed $U_{g,0} = 10.3\,\mathrm{m\,s^{-1}}$, or $U_{g,0}/c = 0.72$, and γ is a constant. Shown in Fig. 12 is the form drag derived from group A, B, and C simulations versus the product of wave speed, wave slope, and geostrophic wind difference, $U_g - U_{g,0}$. Also included in Fig. 12 is the line corresponding to (8) with $\gamma \approx 0.003\,67$. The empirical constant γ is obtained by linear least squares fitting using data from the simulations in groups A, B, and C. For the parameters examined in this study, the magnitude of the form drag calculated from (8) is substantially larger than the wave-induced stress calculated using $D_p = (1/2)c_\beta(ak)^2u_*^2$, where for fast waves, the constant $c_\beta \approx -32$ (Hanley and Belcher 2008). The wave-induced stress can be related to the swell growth rate through $D_p = \beta_g\rho_w ga^2/2\rho_a c$ (e.g., S09). Using (8), we obtain the swell growth (damping) rate (β_g),

$$\beta_g = \frac{2\gamma\rho_a(U_g - U_{g,0})}{\rho_w a}. \tag{9}$$

For $a = 2\,\mathrm{m}$, $U_g = 3$, with air density $\rho_a = 1\,\mathrm{kg\,m^{-3}}$ and water density $\rho_w = 1000\,\mathrm{kg\,m^{-3}}$, we have $\beta_g \approx 0.08\,\mathrm{h^{-1}}$, or for $c = 14.3\,\mathrm{m\,s^{-1}}$, an e-folding decay distance of 640 km. Equation (9) also suggests that the decay distance can be significantly longer for a stronger geostrophic wind—that is, a smaller $U_g - U_{g,0}$.

5. Conclusions

The response of the atmospheric boundary layer to propagating swell has been examined based on three groups of LESs over a range of swell parameters and wind speed in the light-wind–fast-wave regime. These simulations suggest that the impact of swell on the boundary layer turbulence and wind profiles varies significantly with swell characteristics. More than half of the simulations produce a wave-driven wind jet associated

with a negative total surface stress as reported in previous studies. The strength and height of the maximum wind speed appear to be sensitive to the swell properties and the geostrophic wind. Analysis of a one-dimensional boundary layer model (i.e., S09) identifies the ratio between the surface shear stress and form drag, $\beta = \tau_{sh}/D_p$, as a key nondimensional parameter determining the wind jet height and strength. According to the S09 model, the necessary condition for the formation of a wave-driven jet is $0 > \beta > -1$. Under this condition, the negative form drag overpowers the surface shear stress, and the wavy surface serves as a momentum source rather than sink to the overlying atmosphere. A smaller $|\beta|$ implies that the form drag is more dominant and accordingly the jet is stronger and the nondimensional jet level is lower. Our LESs are in qualitative agreement with these predictions.

According to these simulations, the form drag linearly increases with the slope and propagation speed of swell. The linear increase of the drag with the wave slope seems to be in contradiction to linear theory, likely because of the relatively steep swell used in our simulations (i.e., $s \geq 0.1$ except for S05). The form drag is found to be linearly dependent on the geostrophic wind speed as well. For given swell, two thresholded wind speeds exist—namely, $U_{g,0}$ and $U_{g,1}$—where $U_{g,0} > U_{g,1}$. For $U_g < U_{g,1}$, the negative form drag dominates the shear stress, the total stress is negative, and consequently a wind jet is present. For $U_{g,1} < U_g < U_{g,0}$, while the form drag stays negative and the magnitude linearly decreases with increasing U_g, the total surface stress becomes positive, and accordingly, no wave-driven wind jet exists. It is worth noting that these threshold wind speeds vary with swell characteristics.

The other important parameter that governs the jet strength and height is the vertical decay distance of the pressure stress L_d assuming that the pressure stress D_p decays exponentially with the vertical distance. The vertical divergence of D_p, which is inversely proportional to L_d, plays an essential role in the momentum balance and, therefore, in shaping the wind and turbulence profiles in the lower boundary layer, especially within the WBL. On the other hand, L_d is largely determined by the swell wavelength. It is challenging to properly represent this closely coupled system in a low-order analytical model, which usually assumes either L_d or the wind profiles are known a priori. Letting $L_d = (\alpha_p k)^{-1}$, the coefficient α_p estimated from our LESs is between 0.5 and 2 and varies with the wavelength, wave slope, and the geostrophic winds.

According to MOST, under neutral conditions, the wind speed profile in the surface layer should follow a log law. In a number of swell simulations, the simulated wind profiles in the WBL follow a log law to a good approximation. For the rest, at least part of the wind profile, typically between 3 and 12 m above the wave surface, still approximately follows the log law. The S09 solution provides a plausible explanation to the existence of the thin log-law layer in the simulated wind profiles in the presence of swell. On the other hand, substantial difference is found between the surface stress derived from the logarithmic wind profile (i.e., u_{p*}^2) and the total surface stress (i.e., the actual air–sea momentum exchange), implying that MOST is generally invalid over a swell-dominated ocean area, even when the wind profile follows a log law. In fact, two critical hypotheses that MOST is based on are violated over swell. First, for the simulations presented in this study, the magnitude of the wave-induced pressure stress may be comparable to the turbulence stress or even larger, and yet there is no proportional relationship between the pressure stress, which is part of the total stress, and the vertical wind shear. Second, the pressure stress has its own vertical length scale, L_d [i.e., $D(z) \sim e^{-z/L_d}$], determined by the wavelength and likely the wind profile. These results caution the use of the profile method for deriving the surface parameters such as surface stress and drag coefficient over ocean waves, even when the observed wind profile closely follows a log law. The obtained drag coefficient or surface stress may not be relevant, unless the validity of MOST can be verified over the study area.

It is also worth noting that the formation of a wind-driven jet tends to create negative wind shear above the WBL where the shear production of turbulence can become larger. Consequently, the swell effects propagate well above the WBL. With strong swell and an intense wave-driven jet, the turbulence aloft may even enhance the boundary layer top entrainment and increase the boundary layer depth.

Finally, we want to emphasize the limitations of this study. While the idealized model configuration greatly simplifies the problem and allows us to focus on some fundamental dynamical processes associated with WBL and swell interaction, it also widens the gap between the modeled conditions and the real world and makes it difficult to validate the model results with observations. For example, Högström et al. (2013) compared observations over the Baltic Sea and a Pacific trade wind site under light-wind and swell conditions. A wind maximum was observed approximately 7–8 m above the sea surface at both sites, and the height of the wind maximum showed little sensitivity to the swell characteristics. More recently, Högström et al. (2015) found that the swell form drag was more sensitive to the significant wave height and less sensitive to the wavelength. These seeming discrepancies between our idealized LESs and

observations could be due to the use of monochromatic waves instead of a continuous wave spectrum in our model or the use of a constant surface roughness length as opposed to that with spatial variation with respect to the swell and temporal variation with sea states. These issues will be addressed in future studies.

Acknowledgments. This research was supported by the Office of Naval Research (ONR) Program Element (PE) 0602435 N. Computational resources were supported by a grant of HPC time from the Department of Defense Major Shared Resource Centers. The authors thank Dr. Jun Zhang from NOAA and two anonymous reviewers for their helpful comments on an earlier draft of the manuscript.

REFERENCES

Belcher, S. E., and J. C. R. Hunt, 1993: Turbulent flow over hills and waves. *J. Fluid Mech.*, **251**, 109–148, doi:10.1017/S0022112093003350.

Carlsson, B., A. Rutgersson, and A. Smedman, 2009: Impact of swell on simulations using a regional atmospheric climate model. *Tellus*, **61A**, 527–538, doi:10.1111/j.1600-0870.2009.00403.x.

Chalikov, D. V., and M. Y. Belevich, 1993: One-dimensional theory of the wave boundary layer. *Bound.-Layer Meteor.*, **63**, 65–96, doi:10.1007/BF00705377.

Cohen, J. E., and S. E. Belcher, 1999: Turbulent shear flow over fast-moving waves. *J. Fluid Mech.*, **386**, 345–371, doi:10.1017/S0022112099004383.

Deardorff, J. W., 1972: Three-dimensional numerical modeling of the planetary boundary layer. *Workshop on Micrometeorology*, D. A. Haugen, Ed., Amer. Meteor. Soc., 271–311.

Drennan, W. M., K. K. Kahma, and M. A. Donelan, 1999: On momentum flux and velocity spectra over waves. *Bound.-Layer Meteor.*, **92**, 489–515, doi:10.1023/A:1002054820455.

Grachev, A. A., and C. W. Fairall, 2001: Upward momentum transfer in the marine boundary layer. *J. Phys. Oceanogr.*, **31**, 1698–1711, doi:10.1175/1520-0485(2001)031<1698:UMTITM>2.0.CO;2.

Hanley, K. E., and S. E. Belcher, 2008: Wave-driven jets in the marine atmospheric boundary layer. *J. Atmos. Sci.*, **65**, 2646–2660, doi:10.1175/2007JAS2562.1.

——, ——, and P. P. Sullivan, 2010: A global climatology of wind–wave interaction. *J. Phys. Oceanogr.*, **40**, 1263–1282, doi:10.1175/2010JPO4377.1.

Harris, D. L., 1966: The wave-driven wind. *J. Atmos. Sci.*, **23**, 688–693, doi:10.1175/1520-0469(1966)023<0688:TWDW>2.0.CO;2.

Högström, U., A. Rutgersson, E. Sahlée, A. Smedman, T. Hristov, W. Drennan, and K. Kahama, 2013: Air–sea interaction features in the Baltic Sea and at a Pacific trade-wind site: An inter-comparison study. *Bound.-Layer Meteor.*, **147**, 139–163, doi:10.1007/s10546-012-9776-8.

——, E. Sahalée, A. Smedman, A. Rutgersson, E. Nilsson, K. Kahama, and W. Drennan, 2015: Surface stress over the ocean in swell-dominated conditions during moderate winds. *J. Atmos. Sci.*, **72**, 4777–4795, doi:10.1175/JAS-D-15-0139.1.

Janssen, P., 2004: *The Interaction of Ocean Waves and Wind*. Cambridge University Press, 300 pp.

Jenkins, A. D., 1993: A simple quasi-linear model for wave generation and air–sea momentum flux. *J. Phys. Oceanogr.*, **23**, 2001–2018, doi:10.1175/1520-0485(1993)023<2001:ASQLMF>2.0.CO;2.

Kihara, N., H. Hanazaki, T. Mizuya, and H. Ueda, 2007: Relationship between airflow at the critical height and momentum transfer to the traveling waves. *Phys. Fluids*, **19**, 015102, doi:10.1063/1.2409736.

Lai, R. J., and O. H. Shemdin, 1971: Laboratory investigation of air turbulence above simple water waves. *J. Geophys. Res.*, **76**, 7334–7350, doi:10.1029/JC076i030p07334.

Moeng, C. H., 1984: A large-eddy-simulation model for the study of planetary boundary-layer turbulence. *J. Atmos. Sci.*, **41**, 2052–2062, doi:10.1175/1520-0469(1984)041<2052:ALESMF>2.0.CO;2.

——, and J. C. Wyngaard, 1988: Spectral analysis of large-eddy simulations of the connective boundary layer. *J. Atmos. Sci.*, **45**, 3573–3587, doi:10.1175/1520-0469(1988)045<3573:SAOLES>2.0.CO;2.

Nilsson, E. O., A. Rutgersson, A. Smedman, and P. P. Sullivan, 2012: Convective boundary layer structure in the presence of wind-following swell. *Quart. J. Roy. Meteor. Soc.*, **138**, 1476–1489, doi:10.1002/qj.1898.

Rutgersson, A., and P. P. Sullivan, 2005: The effect of idealized water waves on the turbulence structure and kinetic energy budgets in the overlying airflow. *Dyn. Atmos. Oceans*, **38**, 147–171, doi:10.1016/j.dynatmoce.2004.11.001.

Semedo, A., Ø. Saetra, A. Rutgeersson, K. K. Kahma, and H. Pettersson, 2009: Wave-induced wind in the marine boundary layer. *J. Atmos. Sci.*, **66**, 2256–2271, doi:10.1175/2009JAS3018.1.

——, K. Sušelj, A. Rutgersson, and A. Sterl, 2011: A global view on the wind sea and swell climate and variability from ERA-40. *J. Climate*, **24**, 1461–1479, doi:10.1175/2010JCLI3718.1.

Smedman, A., M. Tjernström, and U. Högström, 1994: The near-neutral atmospheric boundary layer with no surface shearing stress: A case study. *J. Atmos. Sci.*, **51**, 3399–3411, doi:10.1175/1520-0469(1994)051<3399:TNNMAB>2.0.CO;2.

——, ——, ——, A. Rutgersson, K. K. Kahma, and H. Pettersson, 1999: A case study of air-sea interaction during swell conditions. *J. Geophys. Res.*, **104**, 25 833–25 851, doi:10.1029/1999JC900213.

Sullivan, P. P., and J. C. McWilliams, 2002: Turbulent flow over water waves in the presence of stratification. *Phys. Fluids*, **14**, 1182–1195, doi:10.1063/1.1447915.

——, ——, and C.-H. Moeng, 2000: Simulation of turbulent flow over idealized water waves. *J. Fluid Mech.*, **404**, 47–85, doi:10.1017/S0022112099006965.

——, J. B. Edson, T. Hristov, and J. C. McWilliams, 2008: Large-eddy simulations and observations of atmospheric marine boundary layers above nonequilibrium surface waves. *J. Atmos. Sci.*, **65**, 1225–1245, doi:10.1175/2007JAS2427.1.

——, J. C. McWilliams, and E. G. Patton, 2014: Large-eddy simulation of marine atmospheric boundary layers above a spectrum of moving waves. *J. Atmos. Sci.*, **71**, 4001–4027, doi:10.1175/JAS-D-14-0095.1.

Tennekes, H., 1973: The logarithmic wind profile. *J. Atmos. Sci.*, **30**, 234–238, doi:10.1175/1520-0469(1973)030<0234:TLWP>2.0.CO;2.

Yang, D., C. Meneveau, and L. Shen, 2013: Dynamic modeling of sea-surface roughness for large-eddy simulation of wind over ocean wavefield. *J. Fluid Mech.*, **726**, 62–00, doi:10.1017/jfm.2013.215.